Supplementary Information

Regulating Photocatalysis by External-Stimuli Manipulation of Microenvironment in Europium-Organic Frameworks

*Xin Lu [a], Yi-Fan Li [c], Chen-Li Wang [a], Jing-Yi Gao [a], Yi Zhou *[b] and Chuan-Lei Zhang *[a]*

a. Anhui Provincial Key Laboratory of Advanced Catalysis and Energy Materials, Anhui Ultra High Molecular Weight Polyethylene Fiber Engineering Research Center, School of Chemistry and Chemical Engineering, Anqing Normal University, Anqing 261433, P. R. China. E-mail: clzhang@aqnu.edu.cn.

b. Shandong Engineering Research Center of New Optoelectronic Information Technology and Devices,School of Mathematics and Physics, Qingdao University of Science & Technology, Qingdao 266061, P. R. China. E-mail: zhouyi@qust.edu.cn.

c. School of Environmental and Municipal Engineering, Qingdao University of Technology, Qingdao 266033, P. R. China.

1. Materials and methods.

Materials and Equipment. All chemicals were obtained from commercial sources and used without further purification. Powder X-ray diffraction (PXRD) measurements were carried out on a Rigaku Ultimate-IV X-ray diffractometer using Cu K_α radiation (λ = 1.5418 Å), in which the X-ray tube operating at 40 kV / 40 mA. The infrared absorption spectra of the compounds in the range of 400-4000 cm^{-1} were recorded on a Nicolet (Impact 410) spectrometer using KBr microspheres (500 mg KBr added to 5 mg of sample). A Perkin Elmer 240C elemental analyzer was used for C, H, and N analysis. The synthesized samples were subjected to thermogravimetric analysis (TGA) on a NETZSCH STA 449 F3 simultaneous thermal analyzer at a temperature of 973 K and a heating rate of 10 K min^{-1} under N_2 atmosphere. Low-pressure gas adsorption measurements were performed on a Micromeritics Accelerated Surface Area and Porosity Measurement System (ASAP) 2460 Surface Area Analyzer, and the samples were degassed under dynamic vacuum for 12 hours prior to each measurement. Fluorescence spectra and ion detection were performed on a fluorescence spectrophotometer (model LS 55, Perkin-Elmer). Decay lifetimes were measured in the solid state at room temperature using a FLS920P fluorescence spectrometer from Edinburgh Instruments. Liquid-phase UV-visible absorption spectra were recorded on a Shimadzu UV-2700 spectrophotometer. Solid-state UV-visible absorption spectra were obtained on a Shimadzu UV-3600 spectrophotometer with a $BaSO_4$ white label as a reference. Gas chromatography (GC) measurements were made using a GC-7860 Plus instrument equipped with a thermal conductivity detector (TCD) for H_2 determination and a flame ionization detector (FID) for CO and CH_4 determination. LCMS tests were analyzed on the LCMS-2020. All electrochemical characterization tests were performed on a CHI 660E electrochemical workstation.

Synthesis of DTDA. DTDA ligand was prepared on the basis of palladium-catalyzed cross-coupling reactions as follows. KOH (80 mmol, 5.40 g) was dissolved in 20 ml of ethanol at room temperature with stirring. Then hydroquinone (45 mmol, 5.00 g) was mixed with 20 ml of ethanol and added to the above solution. Further, ethyl bromide (95 mmol, 10.50 ml) was added to the above solution and refluxed by condensation at a temperature of 75°C for 12 hours. After cooling to room

temperature, the ethanol was removed by distillation under vacuum. The solid was extracted with chloroform and water and purified by organic layer concentration and column chromatography to give 7 g of 1,4-dioxobenzene as a white solid (90% yield). 1,4-Dioxobenzene (10 mmol, 1.62 g) was added to 20 mL of glacial acetic acid, and then liquid bromine (20 mmol, 1.80 mL) was added slowly and dropwise through a constant-pressure descending funnel, and stirred for 10 h at room temperature. After filtration through a Brinell funnel, the remaining acetic acid and liquid bromine were removed with saturated $NaHCO_3$ and Na_2SO_3 solutions, respectively. It was washed with deionized water and dried to give 6.84 g of 2,5 -dibromophenyl diethyl ether as a white solid (90% yield). The resulting product (5 mmol, 1.90 g), 4-(methoxycarbonyl)phenylboronic acid (15 mmol, 2.50 g) and K_2CO_3 (15 mmol, 1.75 g) were placed in a two-necked flask protected by nitrogen after evacuation. The catalyst $Pd(PPh_3)_4$ (0.025 mmol, 1.10 mg) was then added and the mixture of 1,4 -dioxane/ H_2O 150 mL (V: V = 3: 2) was injected through a rubber septum. The reaction was then refluxed with stirring at 95°C and the end of the reaction was followed by thin layer chromatography. After cooling to room temperature, 1,4-dioxane was isolated. After extraction, filtration and vacuum concentration, the resulting crude product was purified by column chromatography (silica gel, petroleum ether/ ethyl acetate= 5: 1) to give a white solid. After hydrolysis and acidification, off-white DTDA was obtained (52% yield). MS (EI): m/z = 405 (M^+). Elemental analysis (%): Calcd for $C_{24}H_{22}O_6$, C, 70.94; H, 5.42. Found: C, 70.89; H, 5.35. ^{1}H-NMR (DMSO-d, 500 MHz, 25 °C): 12.95 (s, 2H), 8.01 (d, 4H), 7.75 (d, 4H), 7.56 (s, 2H), 4.66 (t, 6H), 1.58 (q, 4H).

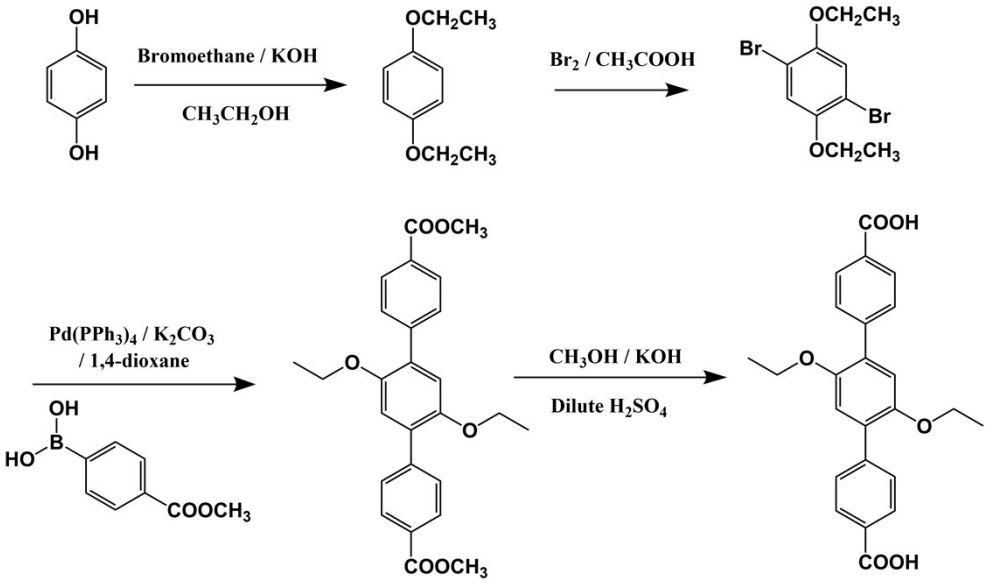

Scheme S1 Synthetic route of DTDA.

Synthesis of Eu-MOF-T. A mixture of DTDA (20.30 mg, 0.05 mmol) and $EuCl_3 \cdot 6H_2O$ (18.67 mg, 0.05 mmol) in a solvent mixture of DMF/ CH_3OH/ H_2O (6.0 ml, v: v, 3/ 1/ 2) was sealed in a Teflon-lined stainless steel autoclave. The reaction was solventothermally reacted at 80°C for 3 days and then slowly cooled to room temperature. A large number of colorless parallelogram shaped crystals were obtained (Fig. S1), filtered, washed with mother liquor and dried under normal conditions. The yield was calculated to be about 65% according to DTDA. Yield is about 65% based on DTDA. Elemental analysis (%): Calcd for $C_{39}H_{57}EuO_{20}$, C, 46.94; H, 5.76, Found: C, 45.31; H, 5.88.

Preparation of working electrodes. First, 2 mg of photocatalyst was dispersed in a mixture of 990 μL of ethanol and 10 μL of Nafion D-521 dispersion to form a homogeneous slurry. 200 μL of the slurry was taken and coated on a 1 cm × 2 cm indium tin oxide (ITO) glass plate and dried at room temperature. An Ag/AgCl electrode was used as the reference electrode, and a platinum plate was used as the counter electrode.

Electrochemical testing. All electrochemical measurements (photocurrent and Mott-Schottky) were performed in 0.2 M Na_2SO_4 aqueous solution (pH = 7) via a conventional three-electrode system at a CHI 660E electrochemical workstation. The working electrode consisted of an ITO glass plate coated with catalyst slurry, the counter electrode was a platinum foil and the reference electrode was a saturated

Ag/AgCl electrode. Mott-Schottky plots were also measured at AC frequencies of 500 Hz, 1000 Hz and 1500 Hz. The three electrodes were immersed in 0.2 M Na_2SO_4 aqueous solution.

Photocatalytic reduction of CO_2 test. First, 100 mg of catalyst was calcined in a vacuum tube furnace under argon atmosphere at different temperatures (100 °C, 150 °C, 170 °C, 190 °C, 200 °C, 250 °C, 300 °C.) for 2 h to obtain activated samples. Then it added 5 mg of catalyst and 5 mg of photosensitizer $Ru(bpy)_3CI_2$ in the photocatalytic reactor, and injected 5 mL of triethylamine and 20 mL of acetonitrile solvent sequentially. After bubbling with high-purity CO_2 for about 20 min to remove O_2 and other gases, the photoreactor was irradiated using a xenon lamp (MC-PF300C) with a 400 nm filter and filled with condensate. The collected gaseous products were detected by gas chromatography and the liquid products were analyzed by mass spectrometry.

2. Experimental data.

Determination of crystal structure. The single-crystal x-ray dataset was measured at 296 K on a Bruker SMART APEX CCD diffractometer using graphite monochromatic Mo K_α radiation (λ = 0.71073 Å, graphite monochromated)[1-2]. Data frames are recorded using the APEX2 program and processed using the SAINT[2] program in the APEX2. Based on the implementation of multiple scanning technology in SADABS[3], absorption correction was performed on the data. Directly solve using SHELXS and perform full matrix least squares refinement on F^2 using SHELXTL software[4]. Squeeze refinement was performed for Eu-MOF-T and Eu-MOF-S using PLATON for its serious disorder, which shows two water molecule in it. The contribution of solvent atoms is included in the experimental formula and formula weight of Eu-MOFs[5]. Crystallographic data for the structures of the Eu-MOFs reported in this paper have been deposited at the Cambridge Crystallographic Data Center through the CCDC.

Tab. S1 Crystal data and structural refinements parameters of Eu-MOF-T and Eu-MOF-S

Complex	Eu-MOF-T	Eu-MOF-S
Empirical formula	$C_{39}H_{57}O_{20}Eu$	$C_{36}H_{34}EuO_{11}$
Formula weight	1018.78	794.59
Crystal system	Triclinic	Triclinic
Space group	*P*Error!	*P*Error!
a / Å	9.4513(4) A	9.57710(10) A
b / Å	15.2354(7)	11.4691(2)
c / Å	18.4015(8)	18.8419(3)
α / °	108.9470(10)	104.5040(10)
β/ °	95.4730(10)	99.9680(10)
γ/ °	93.3720(10)	101.6730(10)
V / Å^3	2483.35(19)	1906.77(5)
Z	2	2
D_{calcd} / g cm^{-3}	1.072	1.384
μ / mm^{-1}	1.465	1.698
F(000)	926	802
θ min-max / °	1.420, 28.392	1.898, 26.371
Tot., uniq. data	18150, 12291	22697, 7625
R(int)	0.0759	0.0438
Nres, Npar	7, 436	0, 436
R_1, wR_2 [$I > 2\sigma(I)$]	0.0426, 0.0843	0.0365, 0.0794
R_1, wR_2 [*all data*]	0.0565, 0.0868	0.0479, 0.0831
GOF on F^2	1.064	1.010
Min. and max resd dens (e·Å^{-3})	-1.027, 1.731	-0.695, 1.353

$R_1=\Sigma||F_o|-|F_c||/|\Sigma|F_o|$; $wR_2=\{\Sigma[w(F_o^2-F_c^2)^2]/\Sigma[w(F_o^2)^2]\}^{1/2}$;

wherew=$1/[\sigma^2(F_o^2)+(aP)^2+bP]$,$P=(F_o^2+2F_c^2)/3$.

Tab. S2 Partial bond angle (°) of complexes Eu-MOF-T and Eu-MOF-S

Angle（Eu-MOF-T）	ω	Angle（Eu-MOF-S）	ω
O(8)-Eu(1)-O(6)	144.61(16)	O(8)-Eu(1)-O(4)#2	148.67(10)
O(8)-Eu(1)-O(1)	73.59(14)	O(8)-Eu(1)-O(1)	79.65(9)
O(6)-Eu(1)-O(1)	140.09(15)	O(4)#2-Eu(1)-O(1)	85.52(9)
O(8)-Eu(1)-O(2)#1	78.94(14)	O(8)-Eu(1)-O(2)#1	73.32(10)
O(6)-Eu(1)-O(2)#1	84.06(14)	O(4)#2-Eu(1)-O(2)#1	136.64(10)
O(1)-Eu(1)-O(2)#1	125.29(13)	O(1)-Eu(1)-O(2)#1	125.01(9)
O(8)-Eu(1)-O(3)	86.90(14)	O(8)-Eu(1)-O(3)#3	86.75(9)
O(6)-Eu(1)-O(3)	88.22(13)	O(4)#2-Eu(1)-O(3)#3	87.38(9)
O(1)-Eu(1)-O(3)	81.95(13)	O(1)-Eu(1)-O(3)#3	140.42(9)
O(2)#1-Eu(1)-O(3)	142.71(15)	O(2)#1-Eu(1)-O(3)#3	85.02(9)
O(8)-Eu(1)-O(4)	123.14(14)	O(8)-Eu(1)-O(5)	121.94(9)
O(6)-Eu(1)-O(4)	81.44(14)	O(4)#2-Eu(1)-O(5)	80.63(9)
O(1)-Eu(1)-O(4)	80.98(14)	O(1)-Eu(1)-O(5)	77.29(9)
O(2)#1-Eu(1)-O(4)	75.93(14)	O(2)#1-Eu(1)-O(5)	78.00(9)
O(3)-Eu(1)-O(4)	138.73(15)	O(3)#3-Eu(1)-O(5)	139.47(9)
O(8)-Eu(1)-O(7)	72.76(16)	O(8)-Eu(1)-O(9)	76.29(10)
O(6)-Eu(1)-O(7)	72.32(16)	O(4)#2-Eu(1)-O(9)	72.69(10)
O(1)-Eu(1)-O(7)	138.52(16)	O(1)-Eu(1)-O(9)	69.52(9)
O(2)#1-Eu(1)-O(7)	70.16(14)	O(2)#1-Eu(1)-O(9)	142.16(10)
O(3)-Eu(1)-O(7)	72.72(15)	O(3)#3-Eu(1)-O(9)	71.18(9)
O(4)-Eu(1)-O(7)	138.66(15)	O(5)-Eu(1)-O(9)	138.45(10)
O(8)-Eu(1)-O(5)	139.79(16)	O(8)-Eu(1)-O(10)	136.04(11)
O(6)-Eu(1)-O(5)	69.26(16)	O(4)#2-Eu(1)-O(10)	69.18(11)
O(1)-Eu(1)-O(5)	71.03(15)	O(1)-Eu(1)-O(10)	140.80(11)
O(2)#1-Eu(1)-O(5)	138.31(16)	O(2)#1-Eu(1)-O(10)	68.12(11)
O(3)-Eu(1)-O(5)	69.91(16)	O(3)#3-Eu(1)-O(10)	69.93(10)
O(4)-Eu(1)-O(5)	69.05(15)	O(5)-Eu(1)-O(10)	69.61(10)
O(7)-Eu(1)-O(5)	126.20(16)	O(9)-Eu(1)-O(10)	125.72(11)

Tab. S3 Partial bond length (Å) of complexes Eu-MOF-T and Eu-MOF-S

Eu-MOF-T	Å	Eu-MOF-S	Å
O(8)-Eu(1)#1	2.337(3)	O(5)-Eu(1)	2.415(3)
O(1W)-Eu(1)	2.574(3)	Eu(1)-O(8)	2.327(3)
Eu(1)-O(2)#1	2.380(3)	Eu(1)-O(4)#2	2.351(3)
Eu(1)-O(4)#3	2.341(2)	Eu(1)-O(1)	2.373(2)
Eu(1)-O(1)	2.304(3)	Eu(1)-O(2)#1	2.377(3)
Eu(1)-O(2W)	2.516(3)	Eu(1)-O(3)#3	2.384(2)
Eu(1)-O(7)	2.340(2)	Eu(1)-O(9)	2.516(3)
Eu(1)-O(3)#2	2.321(3)	Eu(1)-O(10)	2.637(4)

Symmetry Codes for Eu-MOF-T：#1 = − *x* + 2，− *y* + 2，− *z*；#2 = − *x* + 2，− *y* + 2，− *z* + 1；#3 = *x* + 1，*y*，*z* + 1.

Symmetry Codes for Eu-MOF-S：#1 -x+1，-y+2，-z+1；#2 -x+1，-y+2，-z；#3 x+1，y，z+1；#4 -x，-y+1，-z；#5 x-1，y，z-1.

The density functional theory calculations. The density functional theory (DFT) calculations were performed to obtain the electronic structure and the CO_2 reduction pathway of different Eu-MOFs structures. To accurately describe the band gap of materials and assess the energy differences between Eu-MOF-T and Eu-MOF-S structures, the hybrid HSE06 functional[6] with LCAO basis sets was used in QuantumATK package[7] as it has shown success in balancing computational efficiency and accuracy for semiconducting and insulating condensed systems with a high number of atoms[8]. The density mesh cutoff was set to 150 Ha, and the energy convergence criterion was set to 10^{-4} eV. Considering the low computational efficiency of hybrid functionals in structure optimization, the exploration of the CO_2 reduction pathway was conducted using widely accepted Vienna Ab-initio Simulation

Package (VASP)[9] with the computationally cheap Perdew-Burke-Ernzerhof (PBE) functional[10]. The energy cutoff was set to 450 eV, and the atomic positions were allowed to relax until the energy and force were less than 10^{-5} eV and 10^{-2} eV $Å^{-1}$, respectively. All Gibbs free energy in reactions was estimated under zero potential as follows

$$G = E + ZPE - TS$$

where E is the intermediate energy, ZPE is the zero-point energy, T is the reaction temperature which was considered as 300 K here, and S denotes the entropy. For reaction steps that involved H^+ and e^-, the computational hydrogen electrode model developed by Nørskov et al.[11] Vaspkit[12] and bader charge analysis code[13] were used for data processing.

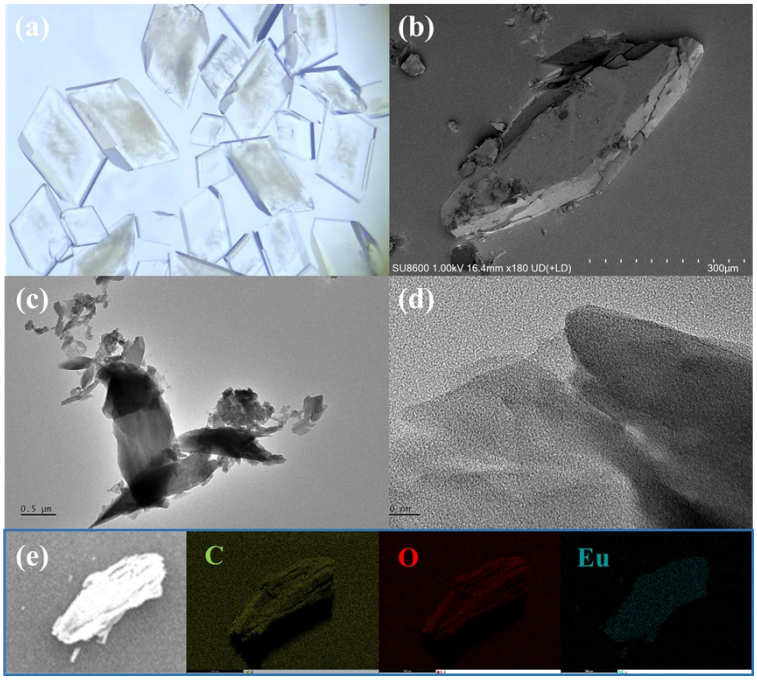

Fig. S1 (a) microscopic images; (b) scanning electron micrographs; (c, d) transmission electron micrographs; (e) mapping of the contained elements of Eu-MOF-T.

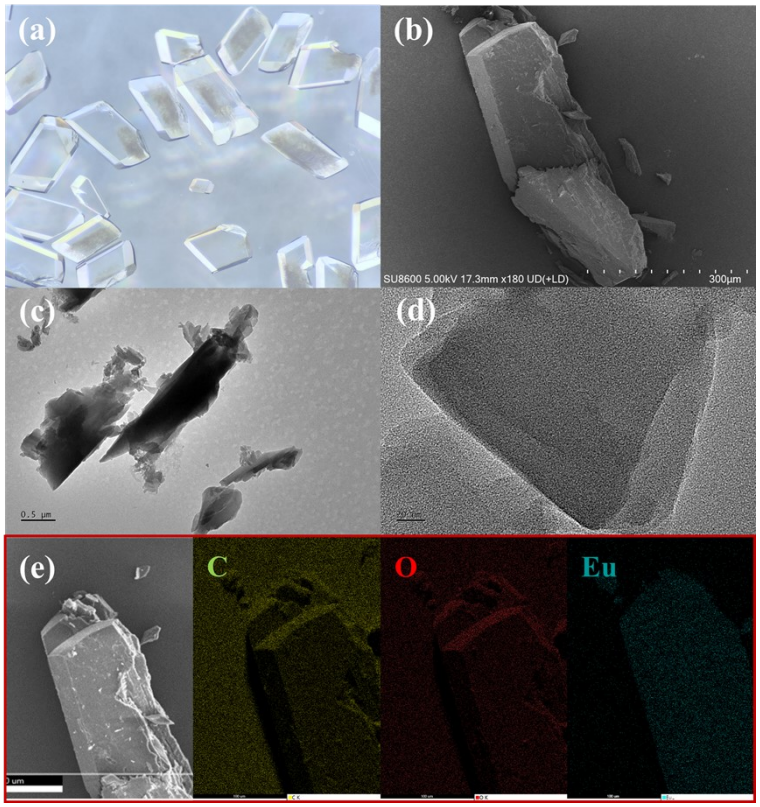

Fig. S2 (a) microscopic images; (b) scanning electron micrographs; (c, d) transmission electron micrographs; (e) mapping of the contained elements of Eu-MOF-S.

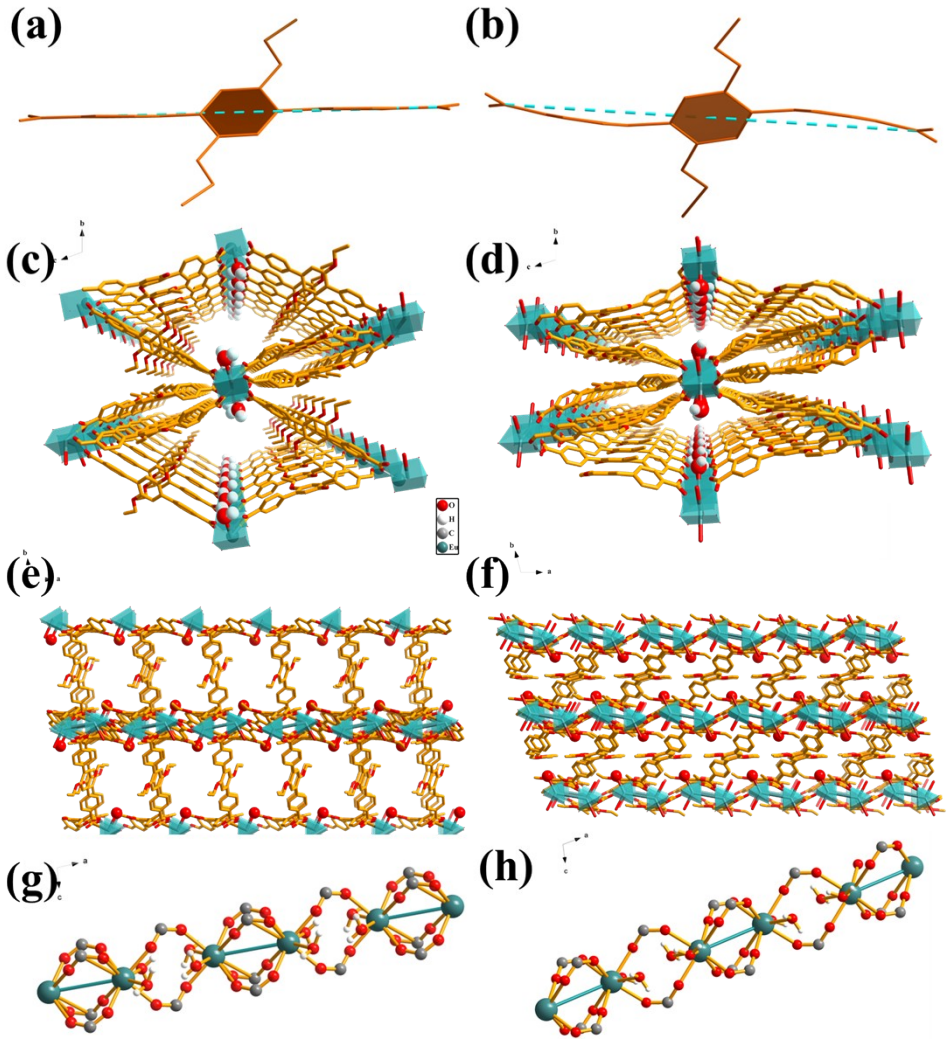

Fig. S3 Degree of ligand torsion of Eu-MOF-T (a) and Eu-MOF-S (b); 3D pore structures of Eu-MOF-T (c) and Eu-MOF-S (d); 3D structural maps of Eu-MOF-T (e) and Eu-MOF-S (f) in c-axis direction; Rod-SBUs plots of Eu MOF-T (g) and Eu MOF-S (h).

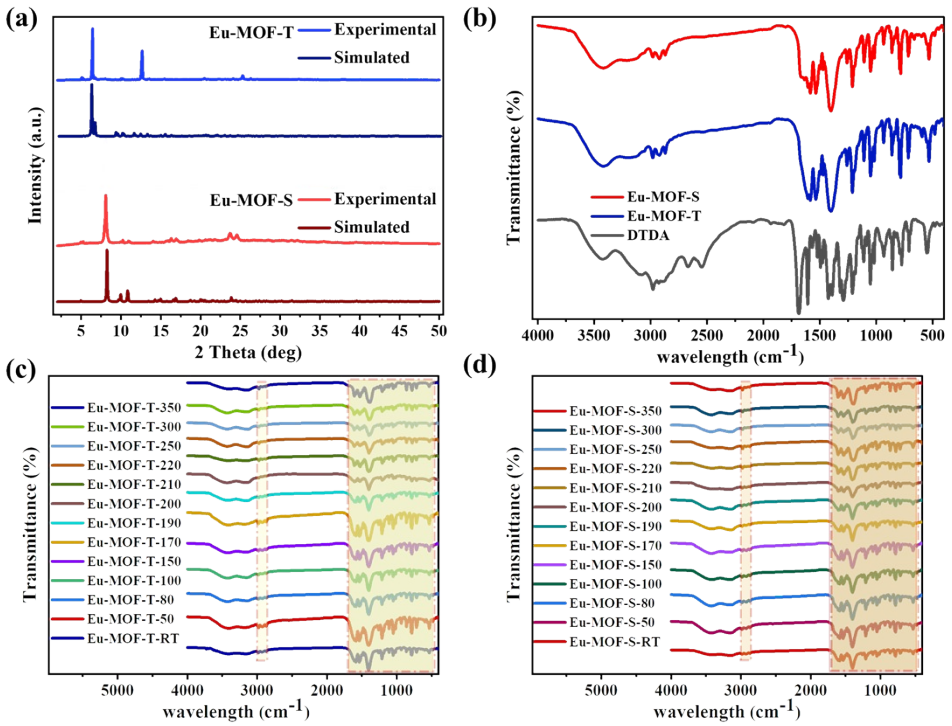

Fig. S4 (a) PXRD spectra of Eu-MOF-T and Eu-MOF-S; (b) IR spectra of Eu-MOF-T and Eu-MOF-S; The infrared spectra of Eu-MOF-T at different temperatures are shown in (c); the infrared spectra of Eu-MOF-S at different temperatures are shown in (d).

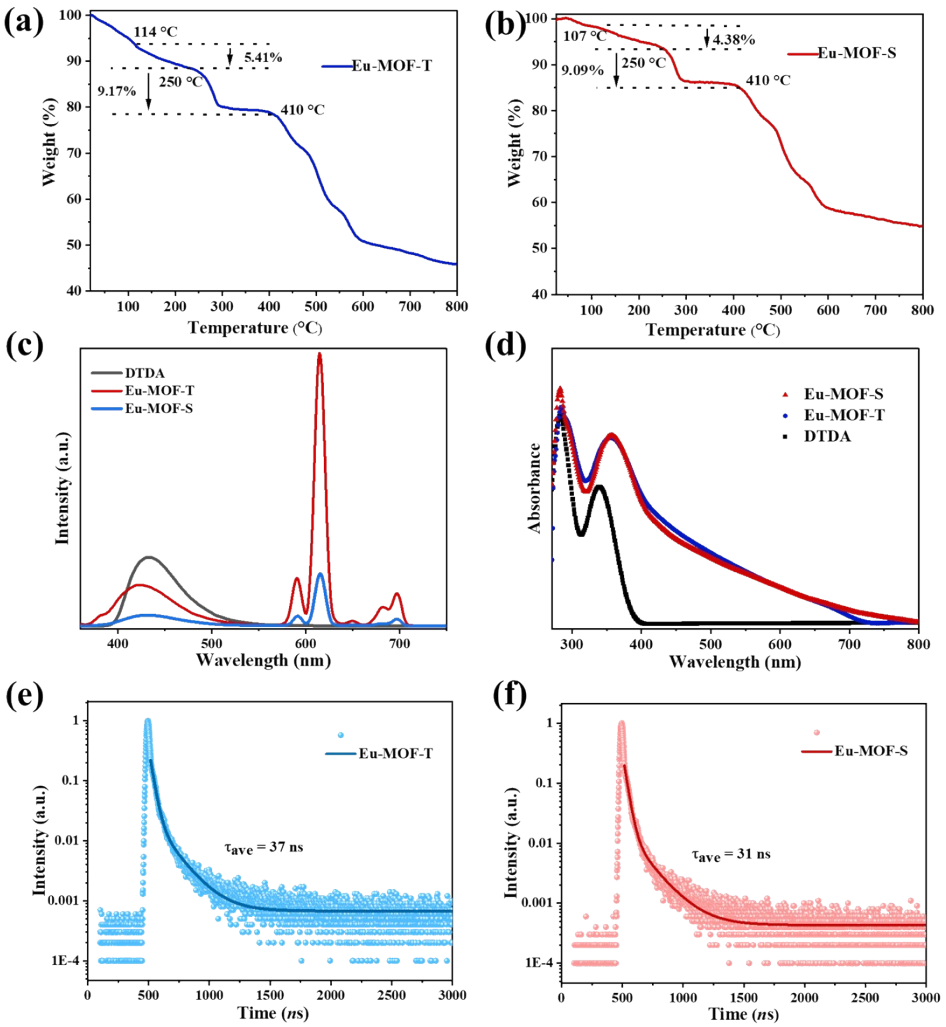

Fig. S5 Thermogravimetric analysis of (a) Eu-MOF-T and (b) Eu-MOF-S (It is the weightlessness of the guest molecules up to 250°C and the coordinating water molecules up to 410°C); (c) Fluorescence emission of Eu-MOFs; (d) UV-visible absorption spectra of Eu-MOFs; Fitted decay curves for (e) Eu-MOF-T and (f) Eu-MOF-S in the solid state at room temperature. Scattered line: experimental data; solid line: fitted by Fit = $A+B_1\times\exp(-t/\tau_1)+B_2\times\exp(-t/\tau_2)$.

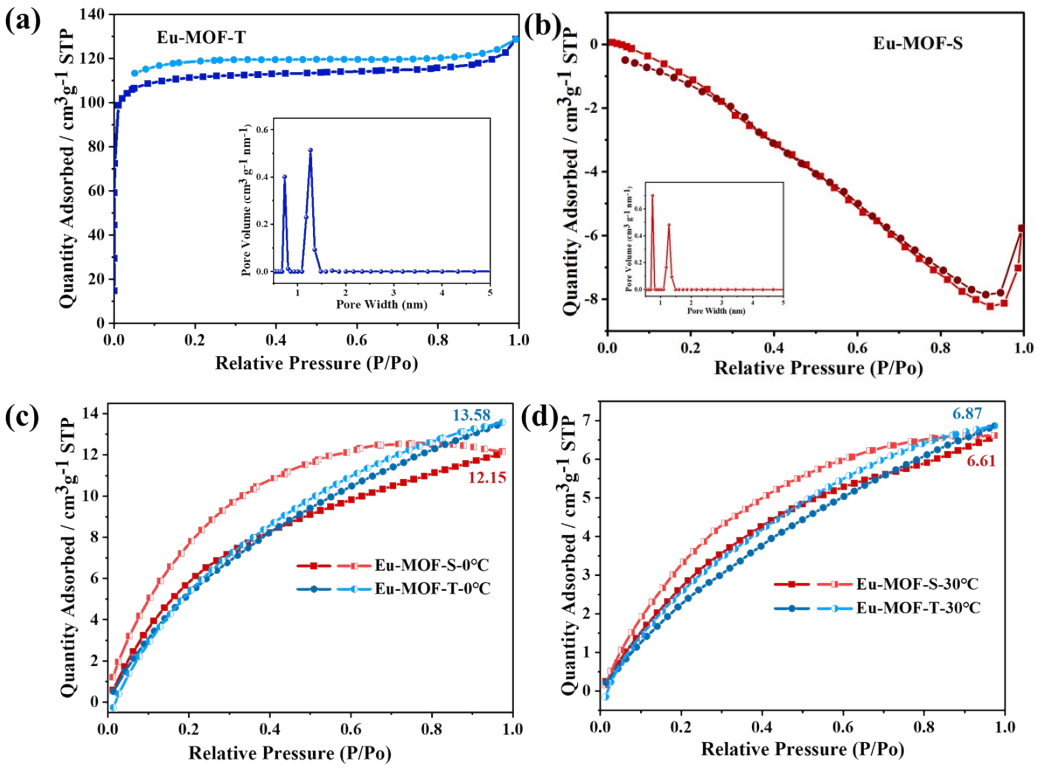

Fig. S6 (a) N_2 adsorption-desorption isotherm of Eu-MOF-T; (b) N_2 adsorption-desorption isotherm of Eu-MOF-S; (c) CO_2 adsorption-desorption isotherm of Eu-MOFs at 0 °C; (d) CO_2 adsorption-desorption isotherm of Eu-MOFs at 30 °C.

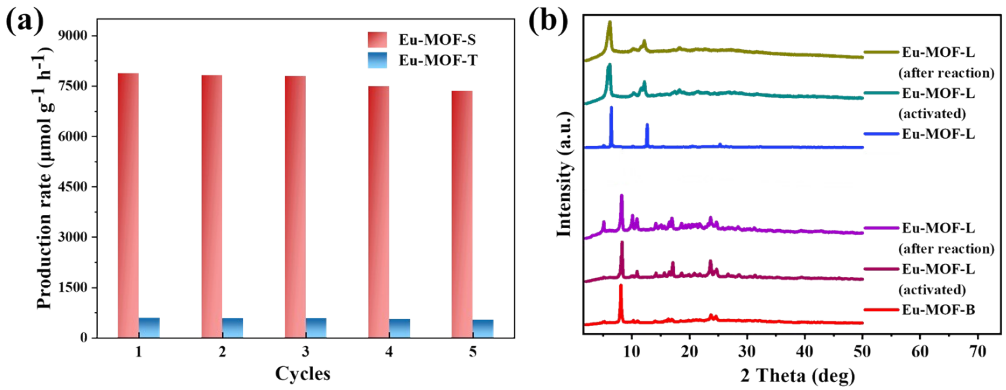

Fig. S7 (a) Photocatalytic CO_2RR cycle test plot of Eu-MOFs; (b) XRD spectra of Eu-MOFs before activation, after activation and after photocatalytic test.

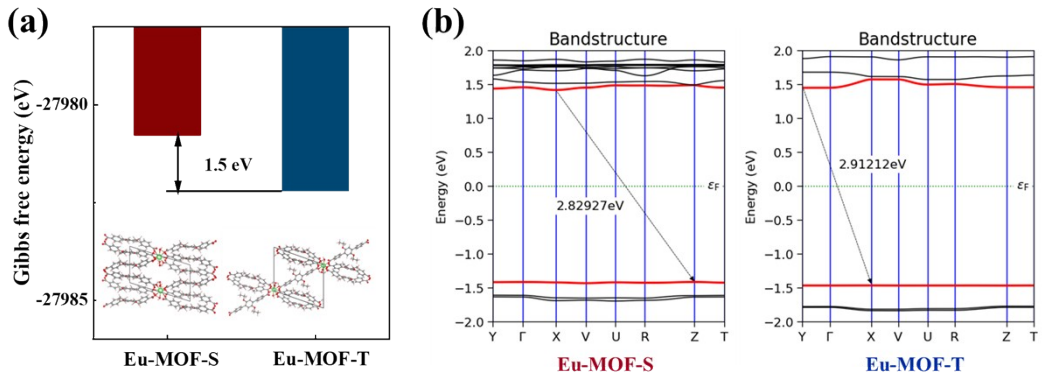

Fig. S8 (a) Theoretical computational units selected for Eu-MOFs and their Gibbs free energies; (b) Theoretical bandgap values of Eu-MOF-S and Eu-MOF-T.

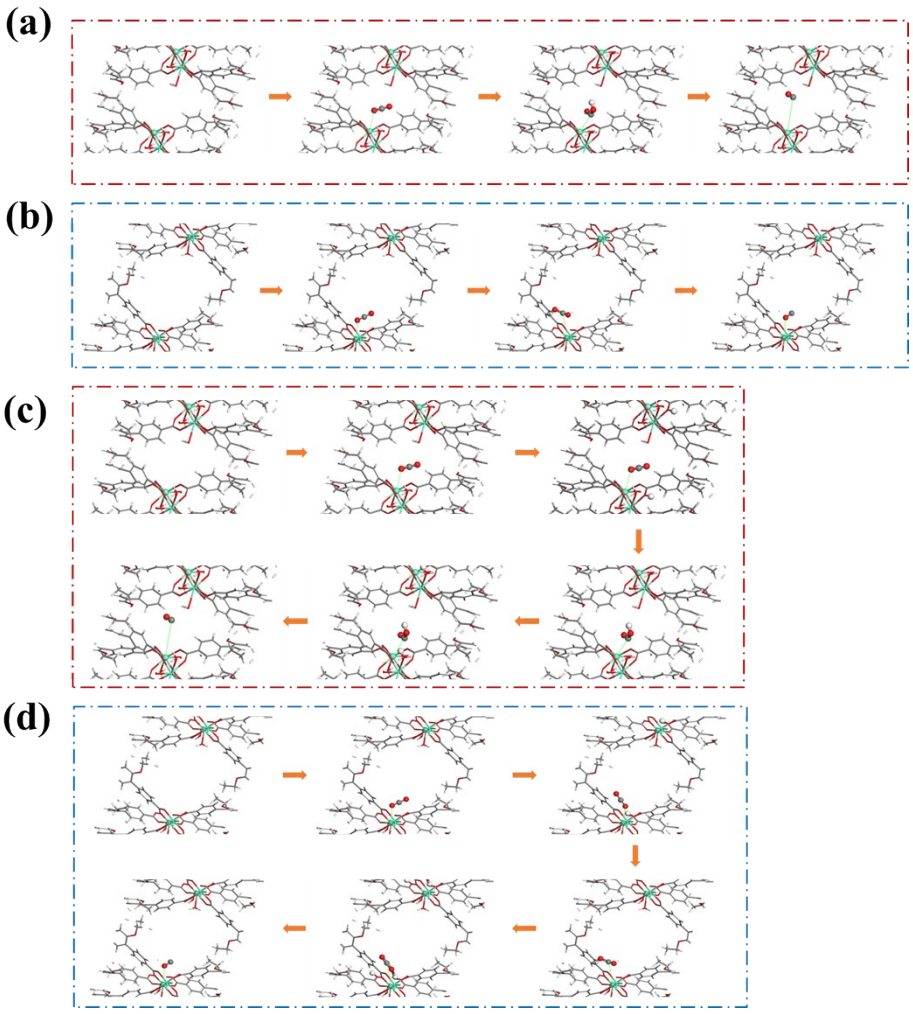

Fig. S9 Structures of reaction intermediates adsorbed on (a, c) Eu-MOF-S and (c, d) Eu-MOF-T as well as electron and proton migration paths throughout the photoreduction of CO_2. The paths in the a, b diagrams are protons from solution, and the paths in the c, d diagrams are protons from adsorbed H^+ in the adsorbed state near the catalytic site.

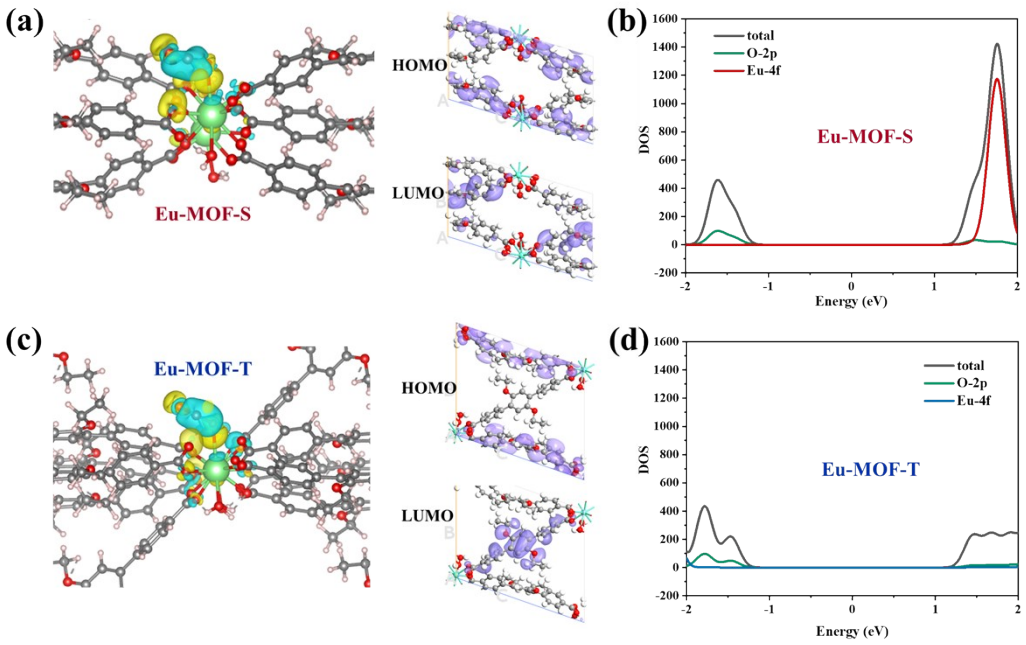

Fig. S10 (a, c) Electron densities of Eu-MOFs as well as HOMO and LUMO; (b, d) DOS of Eu-MOFs.

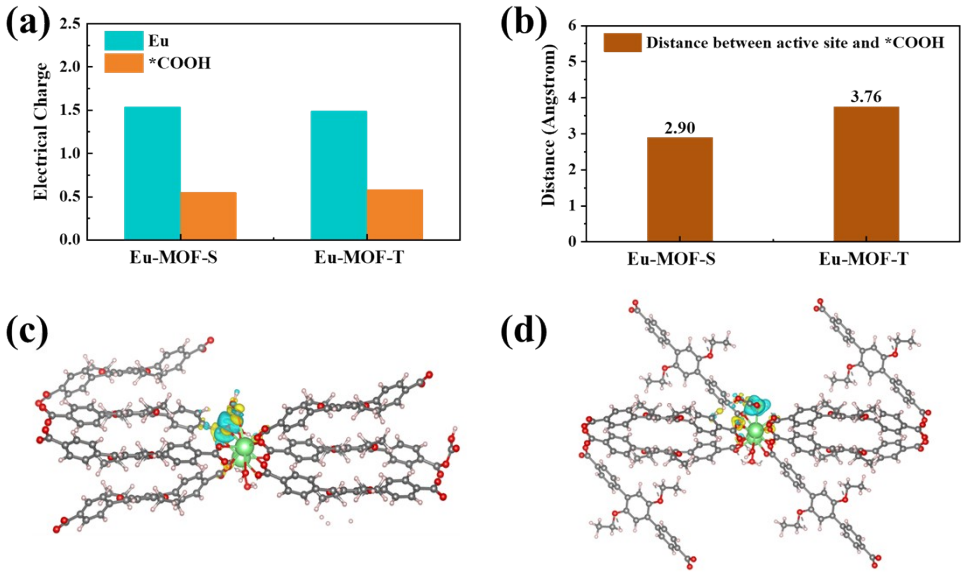

Fig. S11 (a) Electrical charge of *COOH and Eu active site for Eu-MOFs; (b) Distance between *COOH and Eu active site of Eu-MOFs; (c) Differential charge density maps of Eu-MOF-S and (d) Eu-MOF-T.

References

1. Y. Kubota, K. Biradha, M. Fujita, S. Sakamoto and K. Yamaguchi, *Bull. Chem. Soc. Jpn.*, 2002, **75**, 559.
2. SAINT, Version 6.02; Bruker AXS: Madison, WI, 1999.
3. G. M. Sheldrick, SADABS: Empirical Absorption Correction-Program; University of Göttingen: Göttingen, Germany, 1997.
4. G. M. Sheldrick, SHELXTL Reference Manual, Version 6.10; Bruker AXS: Madison, WI, 2000.
5. Gaussian 16, Revision A.03, M. J. Frisch, G. W. Trucks, H. B. Schlegel, G. E. Scuseria, M. A. Robb, J. R. Cheeseman, G. Scalmani, V. Barone, G. A. Petersson, H. Nakatsuji, X. Li, M. Caricato, A. V. Marenich, J. Bloino, B. G. Janesko, R. Gomperts, B. Mennucci, H. P. Hratchian, J. V. Ortiz, A. F. Izmaylov, J. L. Sonnenberg, D. Williams-Young, F. Ding, F. Lipparini, F. Egidi, J. Goings, B. Peng, A. Petrone, T. Henderson, D. Ranasinghe, V. G. Zakrzewski, J. Gao, N. Rega, G. Zheng, W. Liang, M. Hada, M. Ehara, K. Toyota, R. Fukuda, J. Hasegawa, M. Ishida, T. Nakajima, Y. Honda, O. Kitao, H. Nakai, T. Vreven, K. Throssell, J. A. Montgomery, Jr., J. E. Peralta, F. Ogliaro, M. J. Bearpark, J. J. Heyd, E. N. Brothers, K. N. Kudin, V. N. Staroverov, T. A. Keith, R. Kobayashi, J. Normand, K. Raghavachari, A. P. Rendell, J. C. Burant, S. S. Iyengar, J. Tomasi, M. Cossi, J. M. Millam, M. Klene, C. Adamo, R. Cammi, J. W. Ochterski, R. L. Martin, K. Morokuma, O. Farkas, J. B. Foresman and D. J. Fox, Gaussian, Inc., Wallingford CT, 2016, **9**.
6. J. Heyd, G. E. Scuseria and M. Ernzerhof, *J. Chem. Phys.*, 2003, **118**, 8207– 8215.
7. S. Søren, *J. Phys.: Condens. Matter*, 2020, **32**, 015901.
8. T. M. Henderson, J. Paier and G. E. Scuseria, *Status Solidi b*, 2011, **248**, 767-774.
9. G. Kresse and Furthmüller, *J. Comput. Mater. Sci.*, 1996, **6**, 15-50.
10. M. Ernzerhof, and G. E. Scuseria, *J. Chem. Phys.*, 1999, **110**, 5029-5036.
11. J. K. Nørskov, T. Bligaard, A. Logadottir, et al., J. Electrochem. Soc., 2005, **152**, J23
12. V. Wang, N. Xu, J. C. Liu, et al., *Comput. Phys. Commun.*, 2021, **267**, 108033.
13. M. Yu and D. R. Trinkle, *J. Chem. Phys.*, 2011, **134**, 064111.